

# Impact of Formulation and Slurry Properties on Lithium-ion Electrode Manufacturing

Carl Reynolds,<sup>\*[a, d]</sup> Mona Faraji Niri,<sup>\*[b, d]</sup> Marc Francis Hidalgo,<sup>[b, d]</sup> Robert Heymer,<sup>[b, d]</sup> Luis Román,<sup>[c]</sup> Giar Alsofi,<sup>[a, d]</sup> Halima Khanom,<sup>[a, d]</sup> Ben Pye,<sup>[a, d]</sup> James Marco,<sup>[b, d]</sup> and Emma Kendrick<sup>[a, d]</sup>

The characteristics and performance of lithium-ion batteries typically rely on the precise combination of materials in their component electrodes. Understanding the impact of this formulation and the interdependencies between each component is critical in optimising cell performance. Such optimisation is difficult as the cost and effort for the myriad of possible combinations is too high. This problem is addressed by combining a design of experiments (DoE) and advanced statistical machine learning approach with comprehensive experimental characterisation of electrode slurries and coatings. An industry relevant graphite anode system is used, and with the aid of DoE, less than 30 experiments are defined to map impact of different weight fractions of active material (80–96 wt %), conductive additive (Carbon Black at 1–10 wt%) and a two-component binder system (Carboxymethyl Cellulose (CMC) at 1–3 wt% and Styrene Butadiene Rubber (SBR), at 1–7 wt%). Using Explainable Machine Learning (XML) methods, correlations between the formulation, slurry weight percentage (30–

50 wt% in water) and coating speed (1–15 m/min) are quantified. Slurry viscosity, while known to depend on the CMC concentration, is also heavily influenced by carbon black and SBR when at high concentration, as is common in research. Viscosity increasing components also improve adhesion, by improving dispersion and hindering binder migration. Conductivity of the coating on current collector is sensitive to the current collector-coating interface, which makes it a highly useful probe. Improvements in cell capacity are observed with higher viscosity formulations (High weight percentage, CMC content), attributed to reduction in migration and slumping of the slurry on the current collector. SBR had a negative impact at any concentration due to its insulating nature, and carbon black reduces gravimetric capacity when included at high concentrations. The insights from this study facilitate the formulation optimisation of electrodes providing improved slurry design rules for future high performance electrode manufacturing.

## Introduction

According to 2022 reports by BloombergNEF,<sup>[1]</sup> lithium-ion battery (LIB) component prices have increased by 7% from 2021, the first yearly increase in a decade. The average price of

a LIB pack in 2022 was 151 \$/kWh and is soaring due to the rising cost of materials. While material costs dominate the battery production cost, manufacturing processes still represents a significant portion at ~25% of the total cost.<sup>[2,3]</sup> They also represent a significant portion of the energy used, e.g. representing ~66% of the embedded energy in a LMO-Graphite cell.<sup>[4]</sup> Therefore, the LIB manufacturing process still needs to be optimised to minimise costs and CO<sub>2</sub> emissions.

Optimising manufacturing poses significant challenges, primarily due to its complex multi-stage nature and interdependencies between the stages. The current electrode manufacturing process consists of five distinct stages:<sup>[5,6]</sup> (i) formulation involving materials selection and ratio determination, (ii) slurry mixing, (iii) coating the slurry onto a current collector, (iv) drying to eliminate the solvent, and (v) calendering, which compresses the electrode to reduce porosity. Understanding the precise impact of each of these stages on the final electrode and cell performance is challenging, as they have knock-on effects on subsequent processing steps. Thus, there is an essential requirement for systematic generation of experimental data and the development of process models to comprehensively grasp these intricate relationships. The systematic and model-based manufacturing for rechargeable energy storage devices and particularly lithium-ion batteries has been a new topic to the field. The data driven models for capturing the dependency of the mixing,<sup>[7]</sup> coating process,<sup>[8,9]</sup>

- [a] Dr. C. Reynolds, G. Alsofi, H. Khanom, B. Pye, Prof. E. Kendrick  
School of Metallurgy and Materials, University of Birmingham, Elms Rd, Birmingham B15 2SE, United Kingdom  
E-mail: c.reynolds@bham.ac.uk  
Homepage: <https://research.birmingham.ac.uk/en/persons/carl-reynolds>
- [b] Dr. M. Faraji Niri, Dr. M. F. Hidalgo, R. Heymer, J. Marco  
Warwick Manufacturing Group, University of Warwick, Coventry CV4 7AL, United Kingdom  
E-mail: mona.faraji-niri@warwick.ac.uk  
Homepage: <https://warwick.ac.uk/fac/sci/wmg/people/profile?id=1870481>
- [c] Dr. L. Román  
London Centre for Energy Engineering, School of Engineering, London South Bank University, 103 Borough Road, London, SE1 0AA, UK
- [d] Dr. C. Reynolds, Dr. M. Faraji Niri, Dr. M. F. Hidalgo, R. Heymer, G. Alsofi, H. Khanom, B. Pye, J. Marco, Prof. E. Kendrick  
Faraday Institution, Campus, Quad One Becquerel Avenue Harwell, Didcot OX11 0RA, United Kingdom

 Supporting information for this article is available on the WWW under <https://doi.org/10.1002/batt.202300396>

 © 2023 The Authors. *Batteries & Supercaps* published by Wiley-VCH GmbH. This is an open access article under the terms of the Creative Commons Attribution License, which permits use, distribution and reproduction in any medium, provided the original work is properly cited.

calendering,<sup>[10–12]</sup> drying<sup>[13,14]</sup> and electrolyte injection<sup>[15]</sup> are shown to perform well in laboratory and pilot scale manufacturing. These studies try to quantify the effect of some of the critical decision factors, such as coating speed, coating gap, calendering pressure, calendering roll temperature, drying air speed and temperature, on the responses (such as coating porosity, coating thickness) at the end of each step and investigate that further towards the cell characterisations (such as capacity, internal resistance). Although some key results are reported in this context, still many of the manufacturing steps and their extensive set of parameters are not studied sufficiently.

During the formulation stage, the selection of materials and their respective ratios for the electrode takes place. Electrodes typically consist of the active material, conductive additive, and one or more binders. The choice of the active material depends on the desired cell chemistry. Presently, widely used industrial lithium cathodes include Nickel Manganese Cobalt Oxides (NMC) and Lithium Iron Phosphate (LFP), while graphite-based materials are commonly employed for lithium-ion anodes.<sup>[5,6,16]</sup> The conductive additive, usually carbon black, is a fine-particle conducting material that forms a conductive network within the electrode, thereby enhancing its electronic conductivity. Binders, which are typically polymeric materials, play a crucial role. Polyvinylidene Fluoride (PVDF) is commonly used, necessitating the use of N-methyl pyrrolidone (NMP) as a solvent to dissolve the binder and create the electrode slurry. While this solvent-based system is still utilised for NMC cathodes, graphite anodes have transitioned to water-based processing. To replicate the performance of PVDF, a combination of water-based binders is employed. Common water-based binders in the industry include carboxy methyl cellulose (CMC), which is water-soluble and acts as a thickening agent, facilitating suspension, and styrene-butadiene rubber (SBR), which is suspended in water and imparts flexibility and adhesion to the electrode upon solvent removal. However, the adhesion of water-processed electrodes remains notably lower than those made with NMP. This weak interface can result in delamination caused by volume expansion and contraction during cell cycling, leading to premature cell failure.<sup>[17,18]</sup> Furthermore, the presence of non-conducting SBR can limit the rate performance by reducing the overall electrode conductivity. Consequently, the chosen formulation represents a balance between these two factors, and the performance compromise must be carefully evaluated considering the cost and environmental benefits associated with water-based processing. A comprehensive understanding of the relationship between formulation, electrode conductivity, and adhesion is essential for optimizing electrode manufacturing, particularly when water is used as the solvent.

The chosen materials are combined with a solvent to form a slurry. Various mixing equipment or extruders can be utilised, with the ratio of ingredients and solids content affecting mixing efficiency.<sup>[19,20]</sup> Inefficient mixing results in larger particle sizes, leading to coating defects. Poor distribution of the conductive additive and binder can also cause inadequate conductivity and adhesion, respectively.<sup>[21]</sup> The slurry is then coated onto a

current collector, typically copper foil for anodes and aluminium foil for cathodes. Slot die coaters are commonly employed in the industry, although comma bar and blade coating methods are also used on lab and pilot scales. The coatweight and uniformity of the coating must be maintained to a tight tolerance, as the anode and cathode must be balanced in the final cell. The rheology and interfacial properties of the slurry, such as surface tension impact the coating parameters alongside the coating gap and material flow rate. High surface tension produces higher thickness and coatweight as the slurry ‘beads up’ on the surface, but spreads out when the surface tension is low.<sup>[7]</sup> The coating is subsequently dried in ovens to remove the solvent, with careful attention to drying temperature to prevent binder migration and ensure good adhesion.<sup>[17]</sup> Calendering is performed to reduce porosity and enhance energy density, although excessive calendering can hinder ion transport. The preceding stages influence calendering, requiring efficient binder distribution for flexibility and resistance against cracking/delamination.<sup>[12,22]</sup> Due to numerous interdependencies in the process, extracting relationships becomes complex. Detailed information on the challenges can be found in recent battery manufacturing roadmaps,<sup>[23]</sup> review articles<sup>[24,25]</sup> and mapping studies.<sup>[26]</sup>

Investigating the impact of formulation and control variables on slurry and electrode characteristics through experimental methods is vital but challenging and costly, especially in large-scale manufacturing. Thus, modelling approaches are needed to overcome these limitations. Physical models have been employed for specific stages, such as discrete element modelling for structure evolution in calendering,<sup>[27]</sup> and computational fluid dynamics for air entrapment in coating.<sup>[28]</sup> However, combining stages increases complexity, and physical models often rely on empirical data from specific experiments. Data-driven models offer an alternative, less computationally complex method to explore the process, providing insights into the dependencies of manufacturing outputs on physical properties.

Gathering the necessary data for modelling requires a comprehensive set of representative experiments and appropriate training data due to the large number of factors and nonlinear relationships.<sup>[29,30]</sup> Conducting a full-factorial approach with one variable at a time is impractical due to cost and time constraints. Therefore, a customised design of experiments (DoEs) with a reasonable number of cases is essential. The role of DoEs in analysing LIB manufacturing processes is reviewed and summarised.<sup>[31]</sup>

The limited experimental data makes it a real challenge to correlate the control or compositional factors with the slurry and coating quality. Such relations are hard to track with standard statistical methods such as Pearson Correlations,<sup>[32]</sup> or linear regressions. Latterly, it has been shown that machine learning (ML) algorithms are capable of revealing such interdependencies, and recent investigations based on machine learning techniques for battery manufacturing process are well reviewed already.<sup>[25]</sup> Highlighted is how a selection of regression models such as support vectors machines,<sup>[33]</sup> decision trees<sup>[34]</sup> and neural networks<sup>[35]</sup> when combined with explanation

techniques can reveal the dependency between control and response variables. Explainable Machine Learning (XML) technologies, such as Shapley values<sup>[34]</sup> and its computationally effective version SHAP,<sup>[36]</sup> Accumulated Local Effects,<sup>[37]</sup> and Feature Importance<sup>[38]</sup> XML, not only contribute to the modelling of the process, but also focus on cause and effect, correlation, and dependency analysis for shedding light on the black-box style ML representations.<sup>[8,11]</sup>

Despite advancements in modelling, there are still significant knowledge gaps regarding the battery manufacturing process. To address these gaps, a sequential approach is necessary, studying the processes independently and gradually incorporating complexity to encompass the entire process. This study focuses on investigating the influence of electrode slurry formulation on the physical properties of the slurry and electrode, as well as its contribution to the final cell characteristics. Building upon previous work<sup>[7]</sup> that examined the impact of slurry properties on coating, this study further explores how the desired rheology can be achieved through formulation and its effects on electrochemistry. A typical industrial lithium-ion anode system, specifically graphite, processed in water and prone to poor adhesion and delamination issues, is utilised. Graphite is the most common anode system used for lithium-ion batteries, and hence optimisation of its manufacture has a large potential for impact, reducing scrappage rates and startup times for battery manufacturing lines. Graphite formulations strike a balance between adhesion and conductivity, considering the non-conductive nature of binders added for flexibility and adhesion that can negatively affect electrochemistry. Consequently, systematic studies are essential to comprehend the effects of formulation and processing on adhesion, conductivity, and final electrochemistry. The objective of this study is to elucidate the underlying physical relationships governing electrode coating by expanding the combined experimental-machine learning approach. We extend the scope of the process to include slurry formulation and investigate how its components impart specific properties to the slurry, which, in turn, influence the coating quality. Additionally, we broaden the experimental characterization to encompass extensional rheology, coating adhesion, conductivity, and capacity in a half cell. Finally, the incorporation of Design of Experiments (DoE) facilitates a comprehensive approach from experimental design to data analysis, enabling the extraction of manufacturing relationships.

The structure of the paper is as follows. Firstly, the methodology of the research is given, it covers the design of experiments plan and how the experiments are conducted in the laboratory. The modelling techniques including binary logistic regression for slurry mix quality prediction and multiple linear regression (MLR) and Gaussian process regression (GPR) for slurry and coating characteristic prediction are briefed in this section followed by the machine learning explanation techniques of accumulated local effects and multi-factor dependency plots, and model performance evaluation metrics are also given in this section. The main results and findings are outlined followed by summary and conclusions.

## Methodology

### Design of Experiments Plan and Data Preparation

For the purpose of data capture a "mixture-process optimisation" DoE has been used. To the best of our knowledge, this is the first study in the open literature applying this kind of DoE to understand the combine effect of formulation (mixture effects) with manufacturing operating variables on the lithium-ion battery field.

For this DoE, the 6 input features considered were 4 formulation features (weight percentage of active material, conductive additive, binder 1, and binder 2 in the electrode) and 2 process features (coating speed and slurry solids weight fraction). Mixture features are the components of the formulation and must add up to a constant value (in this case, 100%). Due to this constraint, it is not possible to increase one component without reducing another, restricting the overall design space. Process features are parameters which can be individually varied while maintaining other features constant. These can be actual processes (such as coating speed) or general parameters (weight fraction).

To ensure that models have access to high quality data, the range of the factors and responses have been carefully selected based on the experts' view. Also, each control factor has been considered to have a minimum of 2 break points, for nonlinear and more sensitive responses this has been 3. The data points are designed by the DoE approach considering the levels of the noise in the factor measurements such that a measurable change in the responses is evident given the input factor change. With these considerations the dataset is balanced and spatially distributed for modelling purposes.

In order to analyse the mixture and process features into a single study, an optimal mixture-process design<sup>[39–41]</sup> was created using the software Design-Expert® to generate the list of 46 experiments, listed in Table 1 and plotted in Figure 1. Note that the weight percentages displayed are the actual values from the measured weights of materials, which vary very slightly from the DoE due to weighing errors. The features and levels were set based on experimental know-how. For formulation, all components were included, and the ranges were chosen to span the range between maximising active material and maximising conductive additive and binder. Typically 10% of each binder and conductive additive is the highest used in literature so this was chosen as the limit.<sup>[42–44]</sup> Because a combination of binders is used, a range of 1–3% for CMC was chosen and 1–7% was chosen for SBR, giving a maximum of 10% binder overall. The lower limit for CMC was chosen because higher concentrations were typically too thick to mix. Weight fraction spanned from 30%, a low value where drying time would be extended, to 50%, which from trials of the mixing process is close to the maximum value for graphite to achieve a good dispersion in water. This gave an active material content between 80 and 97%. The interest responses were, Viscosity (Pa.s), Extension Time (seconds), Coating Thickness (μm), Coating Weight (gsm), Peel Adhesion Force (N), Conductivity (S/m), and Capacity at its 3<sup>rd</sup> discharge cycle (mAh)

**Table 1.** Complete design matrix from DoE.

Active Material (Graphite) %	Conductive Additive (Carbon Black) %	Binder 1 (CMC) %	Binder 2 (SBR) %	Solids Weight Fraction %	Coating Speed m/min
88.7	5.3	2.0	4.0	30.4	2
90.9	1.1	1.0	7.0	50.0	15
88.8	7.0	3.0	1.2	30.0	15
88.8	1.0	3.1	7.1	29.9	15
96.9	1.0	1.0	1.1	30.0	15
97.0	1.0	1.0	1.0	49.8	2
89.6	5.5	1.0	3.9	30.1	15
80.0	10.0	3.0	7.0	30.0	2
81.8	10.1	1.0	7.1	29.7	15
91.9	1.0	3.0	4.1	29.6	2
87.2	10.6	1.1	1.1	28.7	2
95.6	1.1	2.3	1.0	30.0	2
84.3	9.9	2.3	3.5	30.1	15
88.3	5.4	2.0	4.3	29.9	2
88.2	5.6	2.0	4.2	30.0	15
88.5	5.6	2.3	3.6	40.4	2
91.0	1.1	1.2	6.7	40.1	15
97.0	1.0	1.2	0.8	39.8	2
88.9	1.0	3.0	7.1	40.0	2
79.6	10.0	3.0	7.4	38.8	15
91.9	1.0	3.0	4.1	39.9	15
95.6	1.0	2.3	1.1	39.9	15
85.2	5.5	2.0	7.3	40.0	15
84.6	10.0	2.3	3.1	40.1	15
84.6	10.0	2.3	3.1	40.0	2
85.4	5.7	2.0	6.9	30.0	15
90.9	1.0	1.0	7.1	29.9	2
88.2	5.5	2.0	4.3	50.0	2
88.7	7.3	3.0	1.0	49.8	2
88.9	1.0	3.0	7.1	49.7	2
89.5	5.5	1.0	4.0	50.0	15
89.5	5.5	1.0	4.0	30.0	2
80.0	10.0	3.0	7.0	50.1	15
82.0	10.0	1.0	7.0	50.0	2
91.8	1.1	3.0	4.1	49.9	15
88.0	10.0	1.0	1.0	50.1	15
95.7	1.0	2.3	1.0	50.1	15
84.5	10.1	2.4	3.0	49.4	15
84.6	10.0	2.3	3.1	49.5	2
88.4	5.5	2.0	4.1	49.7	2
89.3	5.5	1.1	4.1	39.7	15
89.0	7.0	3.0	1.0	40.0	2
82.0	10.0	1.0	7.0	39.2	2
87.4	10.0	1.0	1.6	40.0	15
88.4	5.5	2.0	4.1	40.0	2
85.5	5.5	2.0	7.0	50.1	15

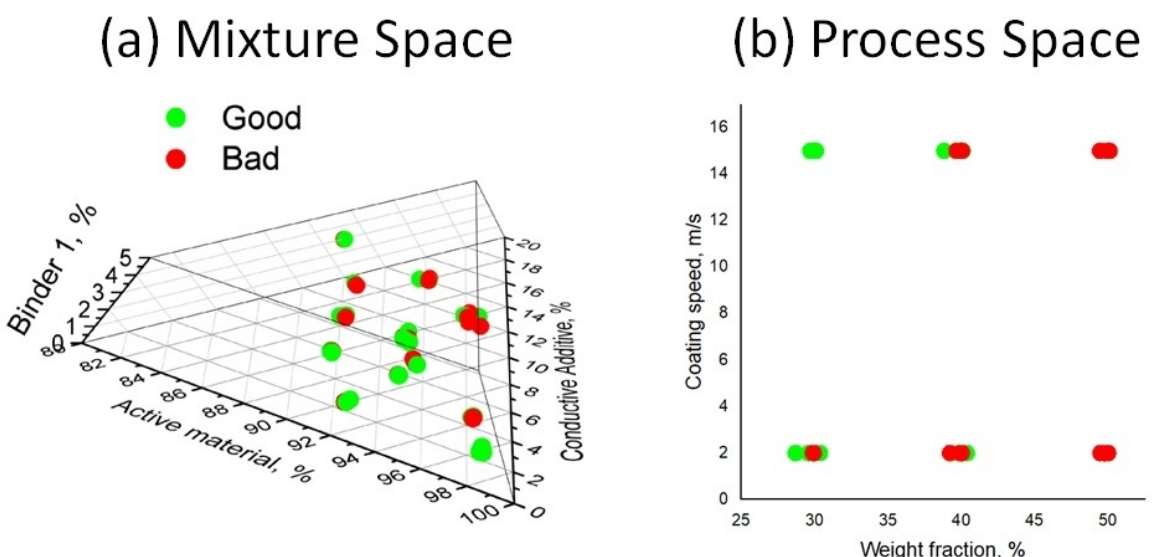


Figure 1. Design space showing (a) the mixture space and (b) the process space (for exact values please refer to Table 1).

which are fully described in the Experiments section. The coating speed range was the upper and lower limit of the draw down coater used (2 m/min to 15 m/min).

Among the 46 points, 20 experiments resulted in unusable mixtures, those colored in red and labelled 'bad' in Table 1 and Figure 1, due to various issues such as difficulties in completely dispersing the solids. Because of this, only the 26 experiments which resulted in usable slurries can be used for modelling responses related to the slurry and electrode properties. The only exception to this is the logistic regression model which will be used to predict whether a slurry will be usable or not. This model uses the entire data set of 46 experiments.

Note that, since the entire data set (which was defined using DoE) will not be used for modelling the slurry and electrode properties, the distribution of the remaining data points need to be evaluated before they are used to create models. Histograms shown in Figure 2 can be used to understand the spread of the new data set. If the shapes of the histograms of the final data sets are similar to the full data sets, then the final data sets can generally be considered balanced and can still be used for further modelling.

The red bars show the counts of the experiments which resulted in unusable slurries. Note that the general distributions of the remaining 26 data points (blue and green) are similar to

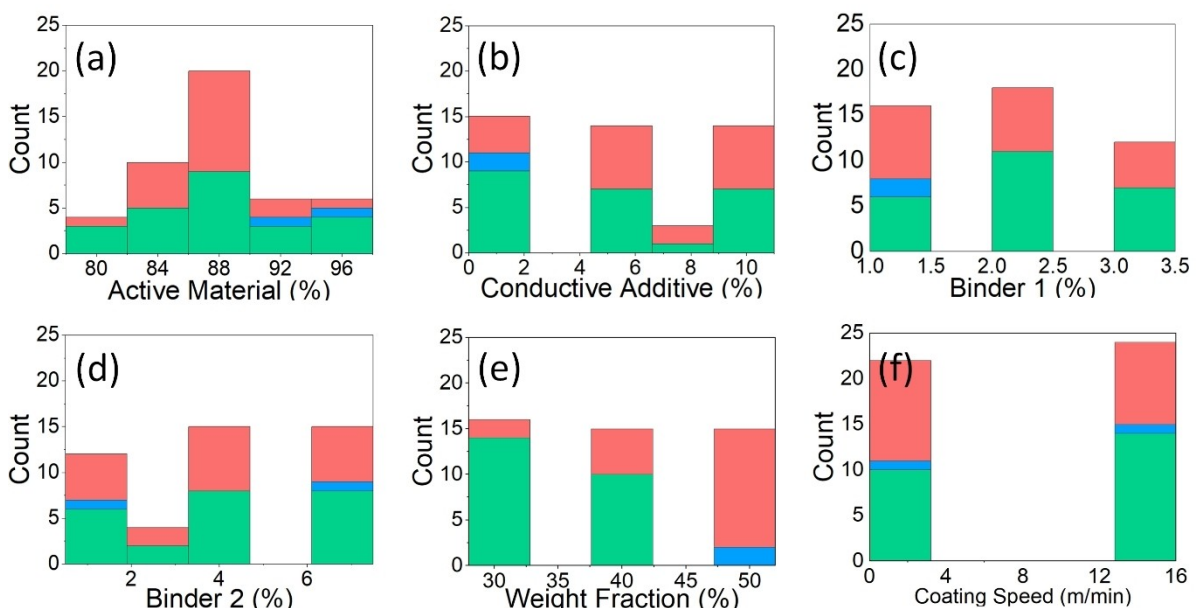


Figure 2. Histograms showing the spread of the data of (a) active material, (b) conductive additive, (c) binder 1, (d) binder 2, (e) weight percent, and (f) coating speed. Red shows the data points which resulted in unusable slurries. The usable slurries with weight percent ~50% are shown in blue. The remaining usable slurries (which were used in the modelling) are shown in green.

the distribution of the entire data set (blue, red, and green), with the exception of weight fraction, where most of the unusable slurries are at ~50% weight fraction. Thus, in order to maintain a balanced data set for weight fraction, all points containing ~50% weight fraction (blue) must also be removed from the 26 usable slurries. The remaining 24 data points are shown in green. In general, the shapes of the green distributions are similar to the shapes of the full data sets. The only exception to this is the weight fraction. However, the weight fraction has a relatively balanced split between the points at ~30% and 40% weight fraction. Thus, the weight fraction data set is still balanced. Overall, even if only a subset of the entire data set can be used for the final modelling, this smaller data set (comprising of 24 experiments) is still a balanced data set and can be used.

Regarding data preparation and cleansing, given the relatively small size of the data, manual data cleansing has been performed to remove the unusable data as described earlier. For the purpose of modelling the data has been normalised to minimise the bias due to the different ranges and scales of control factors that were used as model inputs.

## Experiments

### Materials

The active material for this study was BTR Graphite S360-E3, conductive additive was Imerys carbon black C45, Binder 1 was Ashland carboxymethyl cellulose (CMC), Binder 2 was Zeon Styrene-Butadiene Rubber (SBR) BM-451B (40% suspension in water).

### Mixing

Mixing procedure is kept constant for this study to avoid the relationships becoming too complex, (although the mixing efficiency is changed by changing the formulation).

CMC was pre-dispersed in water at 3.5 weight% using a Silverson overhead mixer for 2 hours.

The slurries were mixed in vials in an Intertronics THINKY mixer. The CMC solution was added followed by the carbon black; this was mixed for 1 minute at 500 rpm followed by 5 minutes at 2000 rpm. The graphite and water (to achieve the desired solids percentage) was then added and the slurry mixed for 1 minute at 500 rpm followed by 10 minutes at 2000 rpm and a 3 minute degas step at 2200 rpm. The SBR was then added before a final mix of 5 minutes at 500 rpm.

The mixing efficiency was measured visually (whether the slurry contained visible unmixed powder or clumps) and by Hegman gauge to evaluate the particle size of the slurry. Slurries that visually were not fully mixed or gave Hegman values above the desired coating thickness (100 micron), were marked as not mixed and not carried forward in the procedure.

### Rheology

A sample of the slurry was characterised using a Netzsch Kinexus Pro Plus rheometer with 40 mm roughened parallel plates. The viscosity was measured between 0.1 and 100 s<sup>-1</sup>, a value near the middle of the range at 1.6 s<sup>-1</sup> was chosen for the machine learning

analysis. Frequency sweeps were performed between 0.1 Hz and 100 Hz at 0.5% strain and a data point at 1.6 Hz chosen for the ML analysis. The central points in the range were selected to avoid some noise encountered at lower rates (particularly for lowest viscosity samples) and avoid any artefacts from inertia at the highest shear rates. To study the SBR solutions alone, viscosity was measured using a 40 mm 2 degree cone and plate, between rates of 2.5 and 100 s<sup>-1</sup> and an average taken. This was not used in the machine learning

The extensional rheology was characterised using a Seymour extensional rheometer constructed in house based on previous designs.<sup>[45,46]</sup> The slurry was loaded to 1.9 mm plates with a separation of 0.5 mm, which was rapidly moved to 5 mm in ~0.005 s. The filament was imaged and the time between the end of the strike and the break-up of the filament measured using in-house MATLAB code, averaged over 3 repeats.

### Surface Tension

Surface tension was measured using a Biolin Scientific Sigma 702 force tensiometer with a Wilhelmy plate. Three measurements were made and averaged for each slurry.

### Coating

Coating was performed using an RK print coat instruments, K Coat paint applicator with a vacuum bed and an Elcometer 3540 film applicator with a 100 micron gap. The slurries were coated onto a copper current collector (PI-KEM 9 micron copper foil, both sides polished). Wet thickness was measured using an Elcometer 3236 wet thickness comb. The coating was dried on a hotplate for 30 min at 50 °C, before being dried in a vacuum oven at 120 °C. The vacuum drying period varied (values given in data table) but was found to have no significant impact on the cell testing or other measured parameters.

The dry coating thickness was measured using a dial gauge, five measurements were made in the corners (approx. ~2 cm in to avoid edge effects) and centre and averaged (Note that the coating thickness later discussed is this uncalendered thickness). The coatweight was measured using a Mesys Ultrasound coatweight measurement system, again five measurements were made in each corner and the centre and averaged. The theoretical densities, of the coatings were calculated from the ratios of added components (Eq. 1), and the thickness and coatweight measurements were then used to calculate porosity (Eq.2).

Theoretical Density,  $\rho_{coating} =$

$$\left( \frac{wt\%_{Graphite}}{\rho_{Graphite}} + \frac{wt\%_{Carbon\ Black}}{\rho_{Carbon\ Black}} + \frac{wt\%_{CMC}}{\rho_{CMC}} + \frac{wt\%_{SBR}}{\rho_{SBR}} \right)^{-1} \quad (1)$$

$$\text{Porosity (\%)} = \left( 1 - \left( \frac{\left( \frac{\text{Coatweight}}{\text{Coating thickness}} \right)}{\rho_{coating}} \right) \right)^* 100 \quad (2)$$

Where  $\rho_{Graphite} = 2.25 \text{ g/cm}^3$ ,  $\rho_{Carbon\ Black} = 1.8 \text{ g/cm}^3$ ,  $\rho_{CMC} = 1.6 \text{ g/cm}^3$  and  $\rho_{SBR} = 0.98 \text{ g/cm}^3$ .

### Adhesion

Adhesion was measured using a 180 degree peel test developed for the Netzsch Kinexus Pro Plus rheometer.<sup>[18]</sup> Coating was attached to the upper and lower Plates as shown in Figure 3. The

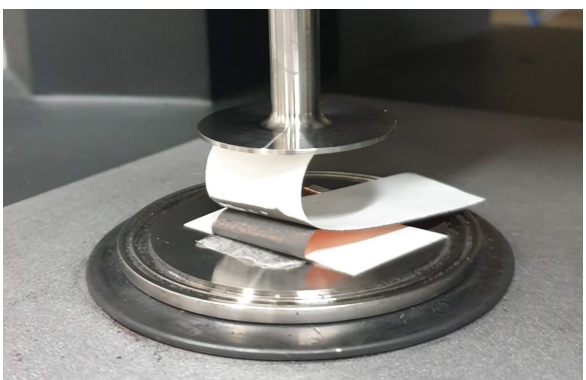


Figure 3. Adhesion Testing with a rheometer.

plates were separated at a speed of 10 mm/s and the axial force transducer of the rheometer was utilised to measure the force as the coating was peeled from the current collector in a 180° configuration. When the force reached a plateau during peeling this value was recorded and 3 repeats were averaged for each coating.

## Conductivity

Conductivity was measured using a Ossila 4-point probe on a 15 mm disc of coating on current collector. Probe spacing was 1.27 mm, tests were run with a target current of 100 mA and a voltage increment of 0.1 V, with a thickness correction factor of 0.942. 50 repeats were performed at the target current and the average value of the conductivity taken for ML.

## Cell Making

The electrodes were tested in coin cells, a subset of 20 of the coatings was chosen due to testing limitations, and three repeats of each were performed. 1 coating (row 45 in Table 1) did not complete formation all cells so was removed and additionally 1 cell did not complete formation for coating 13, leaving 56 cells in total.

The electrodes for cell making were calendered down to a porosity of 30% using an MTI MSK-HRP-01 calender. This was calculated using Eq. 2. The final thickness and porosity values for each coating are given in the attached data table, alongside the coatweight (areal mass loading) for each electrode.

Electrode were cut into 15 mm discs using an EL-CELL electrode cutter and assembled into a coin cell with a glass fibre separator (Whatman GFA). 100 microlitres of electrolyte (1 M LiPF<sub>6</sub> EC:EMC + 2% VC) was added. The counter electrode was a 15 mm lithium disc with a thickness of 150 micron (areal capacity 30.7 mAh/cm<sup>2</sup> using lithium capacity of 3860 mAh/g).

Electrochemical testing was performed at a temperature of 25 °C. Formation was performed between 1.5 V and 0.005 V at C/20. The theoretical capacity was used to determine this rate and was calculated from the active mass of the graphite electrode, assuming a theoretical capacity for graphite of 350 mAh/g (values given in data table).

This was followed by a constant current, constant voltage (CCCV) charge/discharge at C/10, the discharge cycle of which was used to determine the capacity. Gravimetric capacity was calculated by dividing the cell capacity by the active mass (mass of graphite) for the electrode. Capacities and columbic efficiencies for the cycles

are given in the included data table. The raw cell data files are also available on request.

## Modelling and Analysis Methodology

Considering the control factors with levels given in Table 1 and the response variables in the previous section, this section is dedicated to the modelling and analysis techniques of this study. Here three models are developed. A binary logistic Regression model for deciding if the mixture is of acceptable quality or not, the binary model is well suited to categorical predictions with two classes. The other two models are dedicated to predictions (regression). The models are selected as examples of the ML techniques well suited to small datasets. MLR is a first choice as the main purpose has been to investigate if a simple model can provide enough interpretability and predictability for the data. GPR is also selected as is successful in most of the data with normal distributions. The justification behind this choice is now included in the text.

### Binary Logistic Regression

The binary logistic regression function,<sup>[41]</sup> was used to predict whether a slurry was usable or unusable. The model response was set to 1 (if the slurry is usable) and 0 (if not). Then the probability for the slurry to be usable was estimated. As mentioned previously, all 46 data points were used for this model. Specifically, the data was randomly split into an 80–20 training-testing set, with the testing points chosen at random.

### Multiple Linear Regression

In a multiple Linear Regression (MLR) model, the response is calculated as the sum of each feature or interaction multiplied by a coefficient.<sup>[41]</sup> The Kowalski–Cornell–Vining (KCV)<sup>[47]</sup> experimental design able to fit quadratic terms was used in order to model the curvature of the mixture and process features while also limiting the required number of experimental runs.

The model represents the effects from the mixture features, mixture-mixture interactions, mixture-process interactions, and process-process interactions. Note that the sum of the effects from the mixture features and the mixture-mixture interactions models the quadratic mixture effects, meaning that curvature effects due to mixture features can be modelled.

The coefficients model are estimated via minimizing the sum of squares of the errors of each model.<sup>[40,41]</sup> The optimal transformation parameter is also estimated via minimizing the sum of squares of the errors of each model. However, when equal to 1 is within the confidence interval of the minimum transformation parameter, then it is set to 1.<sup>[41]</sup>

Although the KCV mode chosen can in principle fit a quadratic model, in practice, not all terms may be statistically significant which may result in a lower order model. To simplify the model, model reduction is implemented via forward

selection and minimizing the corrected Akaike Information Criterion ( $AICc$ ).<sup>[48]</sup> The base model is the sum of the linear effects of the mixture features. Each regressor is then individually added to the base model, starting with the regressors with the lowest order, and the model with the additional regressor term is fit. The  $AICc$  is then calculated and the model with the smallest  $AICc$  is used as the new base model. This process is repeated until all regressors have been checked. Prior to model parameter fitting, mixture features are scaled from their original units to [0,1]. Process features are scaled from their original units to [-1,1].

For this model, only the 26 successful mixed slurries were used. This works well since the KCV model employed requires a minimum of 19 experiments for fitting.

The analysis of variance (ANOVA) was used to identify the statistically significant model terms and the goodness-of-fit through the  $R^2$  (see 2.3.4). To evaluate the predictive capabilities of the models, the predictive  $R^2$  was used as described elsewhere.<sup>[31]</sup> The F-statistics in the ANOVA table helps in ranking the importance of each term, where higher F-values indicate a higher association with the response.<sup>[7]</sup> In the present work, statistically significant terms were identified by those having a p-value lower than 0.05, and these are shown in the ANOVA tables (see Supporting Information).

### Gaussian Process Regression

Here Gaussian process regression has been chosen to provide further insights to the modelling aspect besides MLR, showcase how the predictability could change from one model to another, and set a basis for comparison.

GPR is a method for non-parametric regression and prediction via prior knowledge in a Bayesian framework as well as the output prediction mean, variance and confidence interval.<sup>[49]</sup> GPR has the ability of uncertainty expression for the predictions<sup>[50]</sup> and rather than postulating a parametric form for the prediction function, and estimating its parameters, it assumes the function as a form of Gaussian process. In fact, GPR has been preferred due to the nature of data that included uncertainties as explained in the previous section. Other models such as random forests, gradient boosted trees or similar could also be practical but exploring them is not the purpose of this paper. Regarding the GPR, considering an input (or feature), a Gaussian process defines a probability distribution of responses over functions.

There exist various options of kernel functions for a GPR model. In this study, the rational quadratic kernel was used, and its hyperparameters were optimised by grid search. The rational quadratic kernel was selected for its ability to capture nonlinear interdependencies, and the models produced using this kernel had better statistics compared to models using other kernels. This and other options of kernel are described by Rasmussen and Williams.<sup>[51]</sup>

In order to calculate the model output, the optimisation of the model's hyperparameters is managed by minimising a logarithmic cost function via gradient descent approach.<sup>[52,53]</sup>

### Model Performance Evaluation

The performance of models described previously is validated using a 80–20 ratio of train and test split of data. The models are trained using the training data set and three complementary accuracy metrics are utilised to evaluate the model's performance only on the validation data. The first metric is the root mean squared error (RMSE) which indicates the difference between the predicted and measured output values across all the range. The second performance metric is R-squared ( $R^2$ ), (also known as goodness of fit<sup>[54]</sup>), This metric includes the sum of the squared error and the total sum of squares obtained for the average of all output values  $R^2$  is a unitless value in the range of 0 and 1, where 1 refers to a perfect prediction performance. The final metric is the mean absolute error (MAE) calculated for all datapoints across the whole range.

While RMSE and MAE are desired to be as small as possible for any models, the closer  $R^2$  to 1 is an indication of a better prediction.

### Impact Analysis and Interpretability

In the formulation and process factor analysis, not only the predictability achieved by model is important but also the possibility of explaining those is desired. While MLR is a white box model with the insights into the contributions of the predictors to the predictions, the more complex machine learning models such as GPR appear as a black box without a possibility to show the impact of each control variable on the response. Here an impact analysis approach from the Explainable Machine Learning context is utilised, which is the accumulated local effects (ALEs).<sup>[36]</sup> Beside that the probability over the entire design space plots, ternary plots, are obtained to highlight the mix impact of more than one control factor in the whole space for each response.

Accumulated local effects are used to relate a particular control variable to a response through the GPR model. In the first order ALE calculation, the impact of one control variable is being quantified for the response regardless of the other control variables. To this aim, the space of control variable is first divided into a limited number of intervals which are specified by some lower and upper limits. After the partitioning of the control variables space, first the model predicts the response based on the actual datapoint, then a prediction with a data point replaced with the lower and upper limit of the interval that covers that datapoint is performed. The difference between these predictions is calculated and used for obtaining an accumulated difference value. Here, the purpose is to quantify the impact of a particular control variable, therefore during each prediction that variable is excluded from the pool of control variables so that its impact becomes clear. To provide a better overview about the strength of the impact of each control variable on the response, the calculated ALE values are all centred. For the multifactor contribution and factor analysis, ternary plots, via the MLR are used. The value of each response is first predicted over the entire design space. Since the MLR

model contains the effects from 4 mixture features, the response prediction, at minimum, requires two ternary plots. Each ternary plot shows the predicted values of a response over all possible combinations of the active material, conductive additive, and binder 2, with one ternary plot showing the predicted response at a low binder 1 level and the other for a high binder 1 level. For each process factor that has a contribution to the overall model, complementary set of ternary diagrams are required. These plots are then used to show changes in the response at all mixture compositions and at different levels of the process features.

For sample-specific explanations SHAP is utilised here.

## Results and Discussion

The results and discussion are separated into the prediction of effective mixing (good or bad) and the effect of the input factors (slurry formulation and weight fraction) on mixing, followed by the model based on the successful mixes/coatings, its parameters and prediction effectiveness, the impact of the

slurry variables on each of several key outputs, and discussion forms the bulk of this section (3.3), with a final summary of the key results (3.4).

### Slurry Quality

Figure 4 maps the probability for the slurry to be mixed (visually containing no unmixed powder with a Hegman gauge particle size under 100 micron) or unmixed over all slurry formulations and at different weight fractions. Here, only 5 of the input variables are considered, as coating speed refers to the subsequent coating of the slurry and thus has no impact on the previous mixing.

The ternary plots show how composition affects the probability of a mixture to be usable (green), unusable (red), or with a 50% probability for to occur (white). Grey regions represent mixtures which are outside the limits of the study. The closer a point is to a specific vertex, the larger the weight % of that compound in the mixture. For example in Figure 4 where Weight Fraction is low and the relative amount of

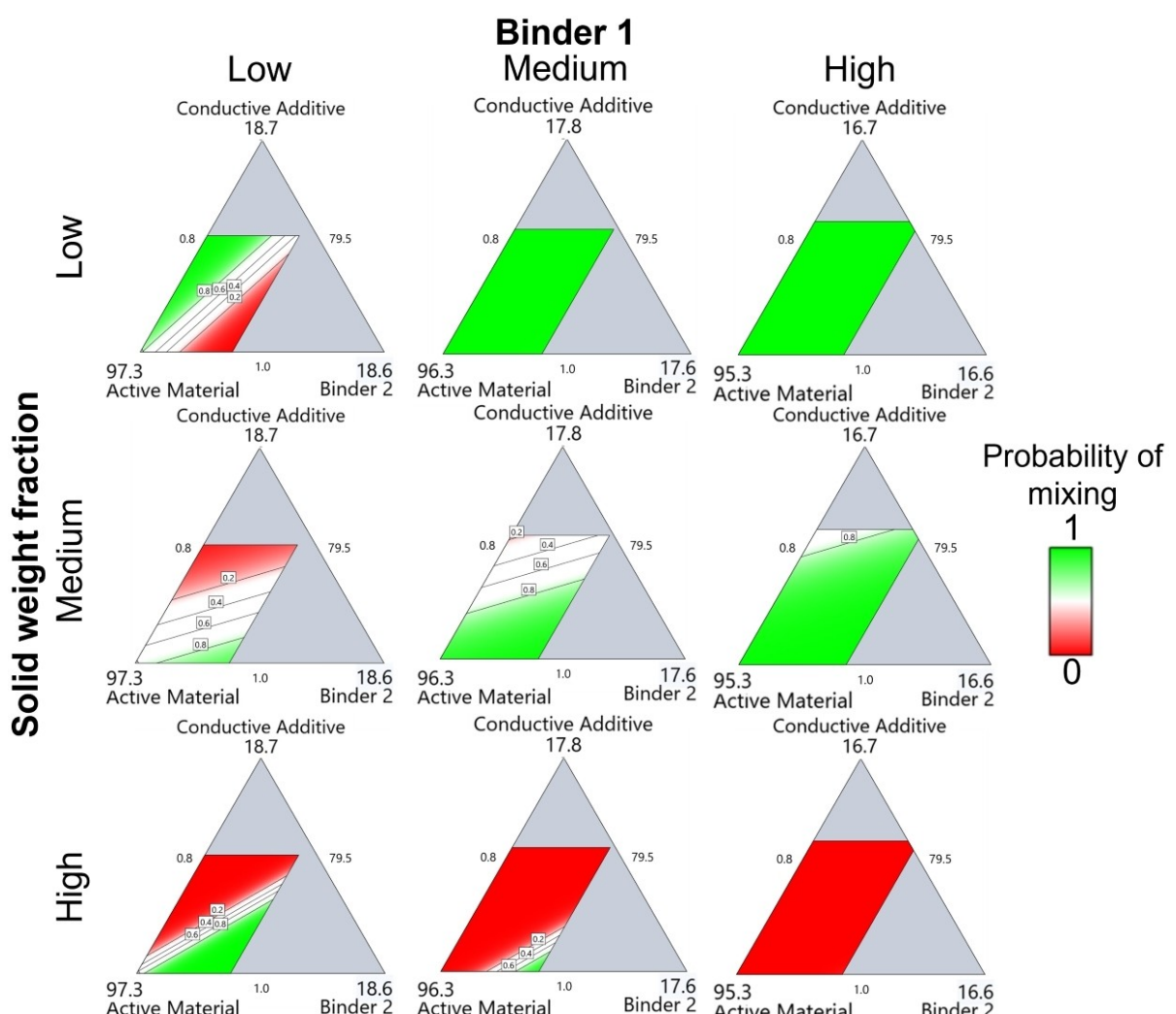


Figure 4. Probability over the entire design space for a slurry to mix (green) or remain unmixed (red).

Binder 1 is low (upper left plot), the green area is mostly on the opposite side of the Binder 2 vertex. This means that when a mixture has a low weight fraction, low amount of binder 1, and low amount of binder 2, it has a high probability of being usable.

In general, as the amount of Binder 1 (CMC) increases, then the probability for the slurry to mix also increases, except when the weight fraction is high. Conversely, decreasing the weight fraction also increases the probability for the slurry to be usable, except when CMC content is low. Although the effect is smaller than that of CMC and weight fraction, in general, having a lower amount of conductive additive also increases the probability to have a usable slurry, except when both CMC and weight fraction are set too low. Therefore, the efficiency of a fixed mixing procedure is a balance between CMC content, weight fraction, and carbon black content.

This can be explained by the competing physical processes to enable efficient mixing. As the mixing process was kept constant, the formulation directly impacts the mixing efficiency (although it should be noted that the slurries that did not perform well here may mixed by more intensive mixing processes). There is an optimum in the viscosity of the wet components for mixing, too low and the particles will settle out and agglomerate,<sup>[55,56]</sup> leading to unmixed clumps in the slurry. Too high and the mixture will not perform well in the planetary mixing process. As there is a limit to the force the mixer can apply, for a given geometry the stress (force divided by area) generated will also be limited, hence increasing the viscosity (the ratio between stress and shear rate), results in a reduction in shear rate, and thus a reduction in mixing efficiency.

The concentration of CMC is therefore key, as this thickens the solvent matrix increasing viscosity and enabling efficient suspension of the active and conductive additive. When this is too low, particles will settle and mixing will be poor, but too high and the wet components are too thick to efficiently mix with the powders. A similar effect is seen for weight percentage, which also causes an increase in viscosity. Carbon black agglomerates in water but may form a network if the concentration is sufficiently high, which will also serve to increase the slurry viscosity, which leads to the small contribution to the mixing efficiency at high contents.<sup>[57,58]</sup>

### Model Response Prediction

Table 2 summarises the results for the MLR and GPR models developed for the prediction of the responses. To provide an overview regarding their accuracy, the distribution of the measured versus the predicted values are given in Figure 5 for four of the seven responses. The graphs are an average of various runs with the data being shuffled from one run to another as explained earlier. The ANOVA tables for each of the responses can be found in the SI, as well as the models.

In Figure 5, the black line is an indicator of the perfect prediction, and the closer the datapoint to that line, the more accurate the prediction. According to the results in Table 2, viscosity and adhesion are most accurately modelled by MLR. Coating thickness, coating weight, conductivity and gravimetric discharge are better modelled by GPR. Extension time is equally modelled by MLR and GPR.

The MLR shows that for all responses, there is always a linear relationship between the mixture formulation components with different levels of impact for each of the responses (as will be described in the next section). The importance of mixture component and process variable interaction can be appreciated from the ANOVA tables. Different responses have different important mixture-process combinations. In general, weight fraction is a more important feature than Coating speed. The two models perform differently for different response due to their different capabilities in dealing with linear and non-linear correlations between the control and response variables as well as relatively small data sizes. GPR is as a whole a better option since provides higher accuracy due to the nonlinear interactions that are present.

### Impact of processing factors and interpretability

In this section, the first and higher order impacts of the control variables on the response are discussed. For the first order impact, the ALE plots from the GPR models are given, centred to the mean value of the predicted response. Each ALE graph shows the impact of that isolated factor on an interest response. The graphs are also include a confidence interval which shows the levels of uncertainty involved in the interpretation of such models. The narrower the bound the

**Table 2.** Prediction accuracy metrics for the MLR and the GPR models.

Metrics Responses and Models	$R^2$		MAE		RMSE	
	MLR	GPR	MLR	GPR	MLR	GPR
Viscosity (s-1)	0.94	0.85	1.06	2.54	3.03	4.04
Extension Time (seconds)	0.89	0.89	0.29	0.03	0.41	0.05
Coating Thickness (um)	0.83	0.92	4.68	2.67	5.23	3.36
Coating Weight (gsm)	0.84	0.88	2.27	2.89	2.98	4.21
Adhesion (N)	0.81	0.79	0.19	0.22	0.24	0.29
Conductivity (S/m)	0.50	0.60	7.1E5	5.1E5	8.7E5	7.1E4
Gravimetric Discharge Capacity (mAh/g <sub>act</sub> )	0.50	0.66	5.14	5.72	7.88	8.64

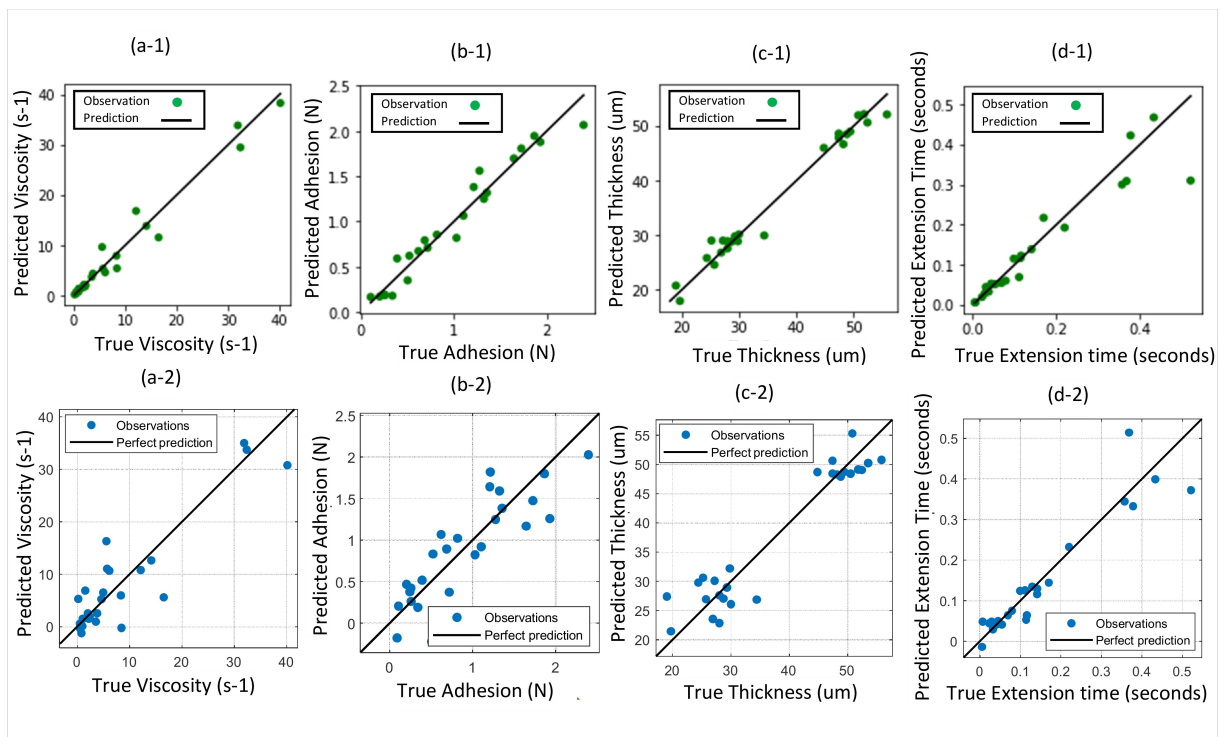


**Figure 5.** The distribution of the predicted versus real values of the Viscosity MLR (a-1), Viscosity GPR (a-2), Adhesion MLR (b-1), Adhesion GPR (b-2), Coating thickness MLR (c-1), Coating thickness GPR (c-2), Extension time to break up MLR (d-1), Extension time to break up GPR (d-2). Green refers to MLR model, Blue the GPR model.

more confidence is there regarding the local impacts of the control factor on the response. Where the models are weaker, such as for conductivity and gravimetric capacity there is also less confidence on the provided explanations.

To study higher order impacts, the ternary plots from the MLR models are presented. As there could exist a larger number of combination of factors for ternary graphs, only a subset is visualised in this study.

The first variable studied is the slurry shear viscosity. As shown in Figure 6(c) and (d), both binders, CMC and SBR increase the slurry viscosity, however the trend is slightly different between them. For SBR until 4% the viscosity is almost unchanged and then a steep increase is witnessed, whereas for CMC, there is a steep increase between 2 and 2.5 wt%. Conductive additive (Figure 6(b)) is seen to increase the viscosity, with a steeper increase at 6 wt% and above, where weight fraction (Figure 4(e)), gives a linear increase in viscosity. While the ALE plots from GPR show individual effects, the ternary plots from MLR show how all the effects of the features come together to affect a specific response. The results from GPR match those from MLR. Figure 6(f) shows that the viscosity increases when Binder 1 (CMC), conductive additive, or weight fraction are increased, or the amount of active material is decreased. It also demonstrates the large effect CMC has on the overall viscosity compared with the other contributions.

The trend with SBR content can be explained by the overlap concentration. The viscosity change with concentration is shown in Figure 7 for SBR (binder 2) alone in water. A steep increase is seen above 10 weight% as the overlap concentration

is reached and the structure changes from small clusters of polymer suspended in solution to a continuous percolated network. Because in the electrode slurries used in this slurry ~30–50% of the weight is other solids, 5–7 weight% SBR would give 10% SBR in the solvent phase. These values are still slightly higher than the 4 weight% where the viscosity begins to increase, so it is likely there is a collaborative effect, and that the conductive additive and active participates in forming a continuous network with the SBR, causing the viscosity increase.

CMC is a much longer chain polymer and is dissolved in solution, and so is above the overlap concentration at all weight percentages used. However, it absorbs to the active material particles, which is likely the reason for the change in gradient above 2% as these interfaces are saturated and so additional polymer goes solely into solution, leading to steeper increases in viscosity.

The conductive additive, Carbon Black is known to form large agglomerates and then percolated networks as concentration increases in water.<sup>[59]</sup> The onset of this agglomeration causes the viscosity increase at 6 wt%. As slurry weight fraction increases there is less solvent present and the components move close together, giving higher resistance to flow and higher viscosity. Active material is also seen to reduce the viscosity, but this is because more active means less space in the formulation for binder and conductive additive, which each increase viscosity.

Figure 8 shows the impact of slurry characteristics on the extension time to breakup for the mixture, a shorter extensional

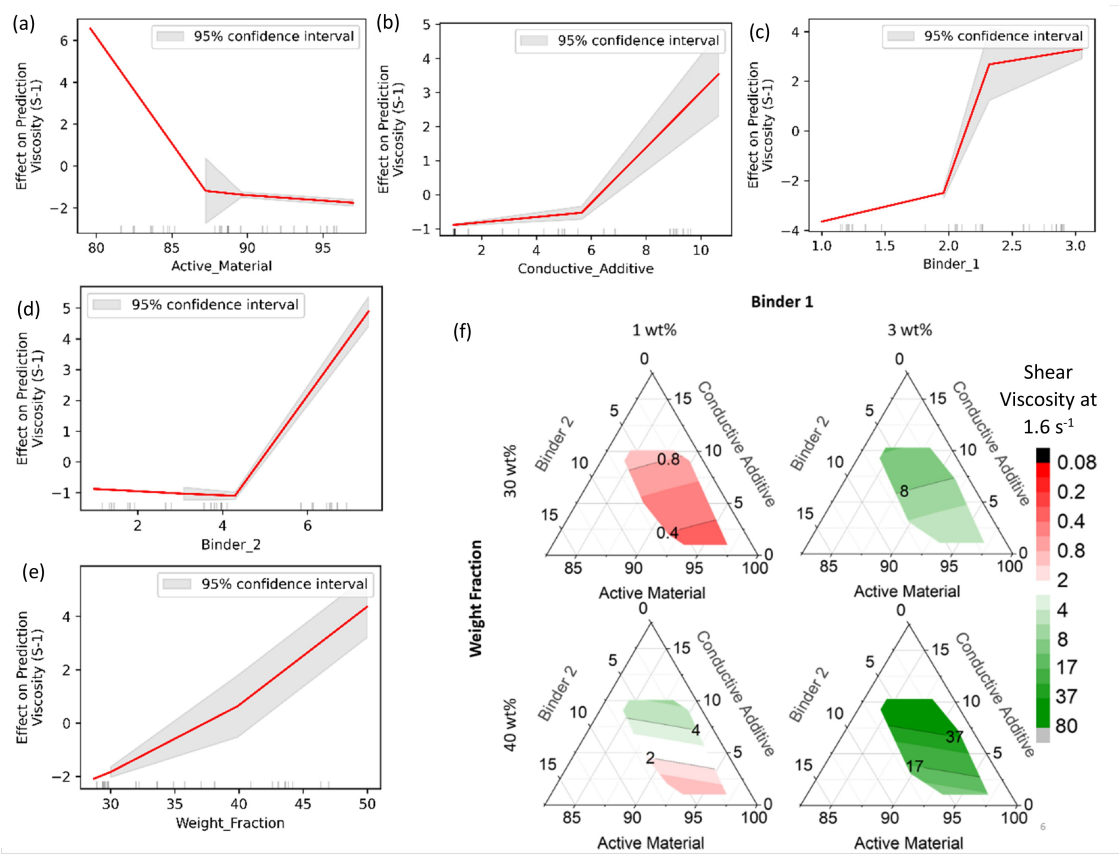


**Figure 6.** First order (a–e) and higher order (f) impact of slurry control variables on the shear viscosity at  $1.6 \text{ s}^{-1}$ .

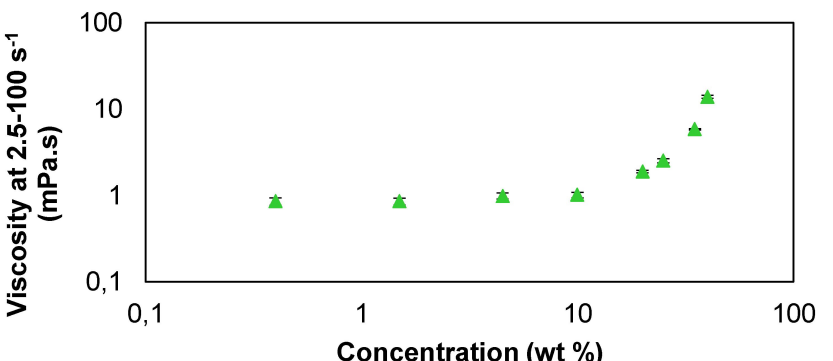


**Figure 7.** Concentration dependence of viscosity of water-SBR (binder 2) solutions (averaged across shear rates from  $2.5$  to  $100 \text{ s}^{-1}$ ) demonstrating an overlap concentration where viscosity increases at high concentrations.

time to breakup implies a lower extensional viscosity. Similar to shear viscosity, CMC, Figure 8(c) and weight fraction, Figure 8(e) have the strongest impact on the extension time. There are subtle differences between the trends in shear and extension, most notably both carbon black and SBR (Figure 8(b) and (d)) do not impact the extension until later weight percentages than in shear (Figure 6(b) and (d)). According to Figure 8(f) the MLR shows similar results. The extension time to break for the mixture increases when the level of CMC is high and when the weight fraction is also set to high.

While there can be different drivers for shear and extensional viscosity, the results suggest for these anode slurries, they are the same. The later onset of the change in extension properties is because extension is sensitive to networks with multiple branch points.<sup>[45]</sup> As the particle concentration increases, the agglomerates grow and form branches (this has been observed for Carbon Black<sup>[59]</sup>). While the presence of agglomerates will affect the shear rheology, it is not until there is a significant amount of branching that the extensional viscosity notably increases. CMC and weight fraction have a synergistic effect. Both features individually increase the

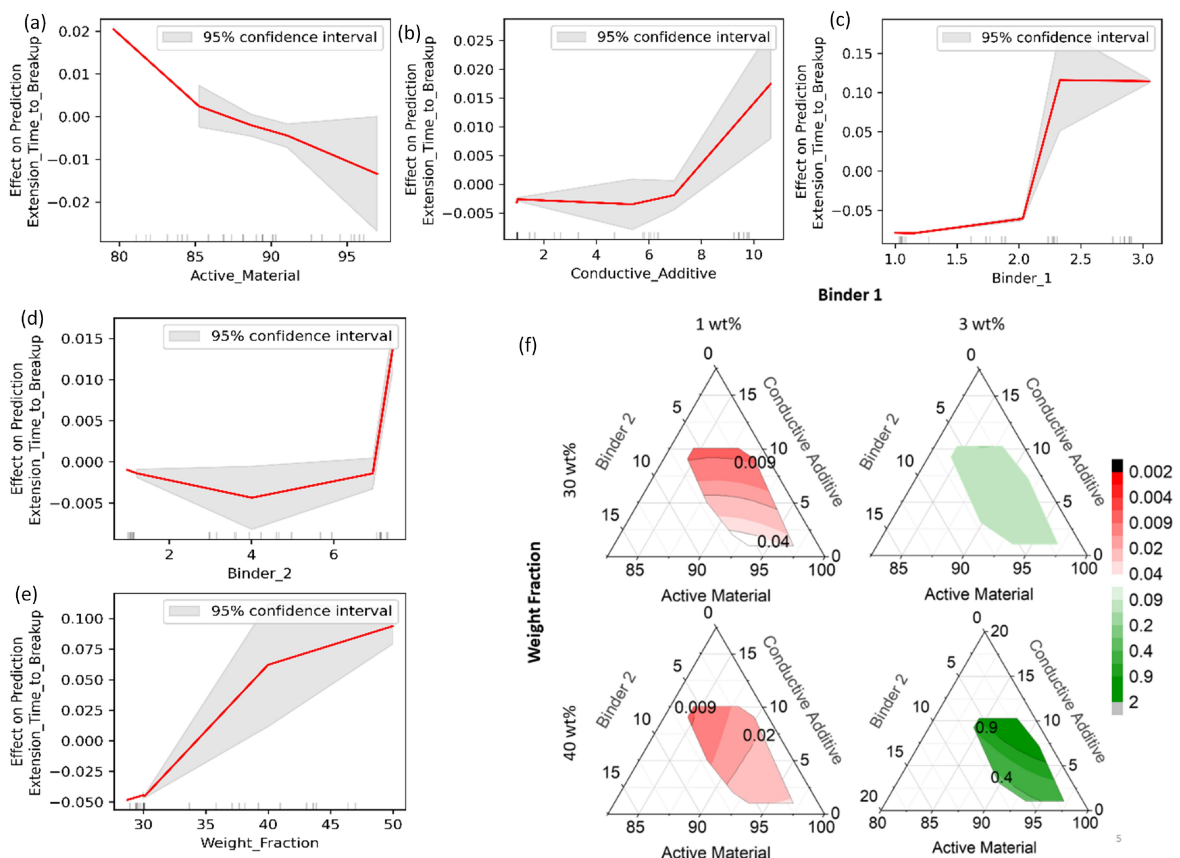


Figure 8. First order (a–e) and higher order (f) impact of slurry control variables on the extension time to breakup.

extension time to breakup. However, when combined, the increase to the extension time to breakup is greater than their individual effects.

Figure 9 summarises the results for the coatweight of the electrode. Considering the range of the ALE values, the weight fraction has the strongest impact, increasing the electrode coat weight, Figure 9(e). Conductive additive, Figure 9(b), decreases coat weight at weight percentages above 4 wt%, the same point it begins to increase the viscosity, decrease with active material weight percentage, Figure 9(a). There is a decrease in coatweight with both CMC Figure 9(c) and SBR content Figure 9(d). The results from the MLR are generally similar in Figure 8(f). Interestingly, weight fraction and the mixture components have interaction effects on coat weight. When CMC and weight fraction are both low, then SBR has a positive effect on the coating weight, whereas when both the CMC content and weight fraction are set to high, then the effect of SBR becomes negative.

The trend with coatweight is expected, as the coatings were made at the same coating gap, so the higher weight percentage slurries which contain less solvent, lead to a higher mass of material in the dry coating.

The correlation between the rise in viscosity and coatweight with conductive additive can be explained by the agglomeration. These agglomerates are more prone to settling in the

vessel (carbon black typically requires surfactant or other stabiliser to prevent settling in water at high weight percentages<sup>[60]</sup>). This settling leads to a depletion in solids in the slurry taken for coating, particularly for formulations otherwise low in viscosity. This also explains why high active material content leads to lower coatweight as it leaves little room in the formulation for components which increase the viscosity and reduce this settling. The trends with SBR and CMC can be explained by density, SBR and CMC have lower density, approximately 1.6 g/cm<sup>3</sup> than graphite (2.2 g/cm<sup>3</sup>) so they reduce the density of the coating and the coatweight. SBR also promotes agglomeration at high weight contents which reduces coatweight.

The interaction effects of CMC, SBR and weight fraction can be explained by viscosity and resistance to settling. When CMC content and weight fraction content is low, overall viscosity is low and so the increase in viscosity provided by the SBR is important to prevent settling. However, when CMC content and weight fraction are high this effect disappears because they both provide larger increases in viscosity.

The effect of slurry properties on adhesion is illustrated in Figure 10. As expected, the rubber binder, SBR, has the largest impact, as shown by the ALE, showing a steep linear increase in adhesion with SBR content (Figure 10(d)). Conductive additive shows a relatively minor effect, but there is a slight decrease

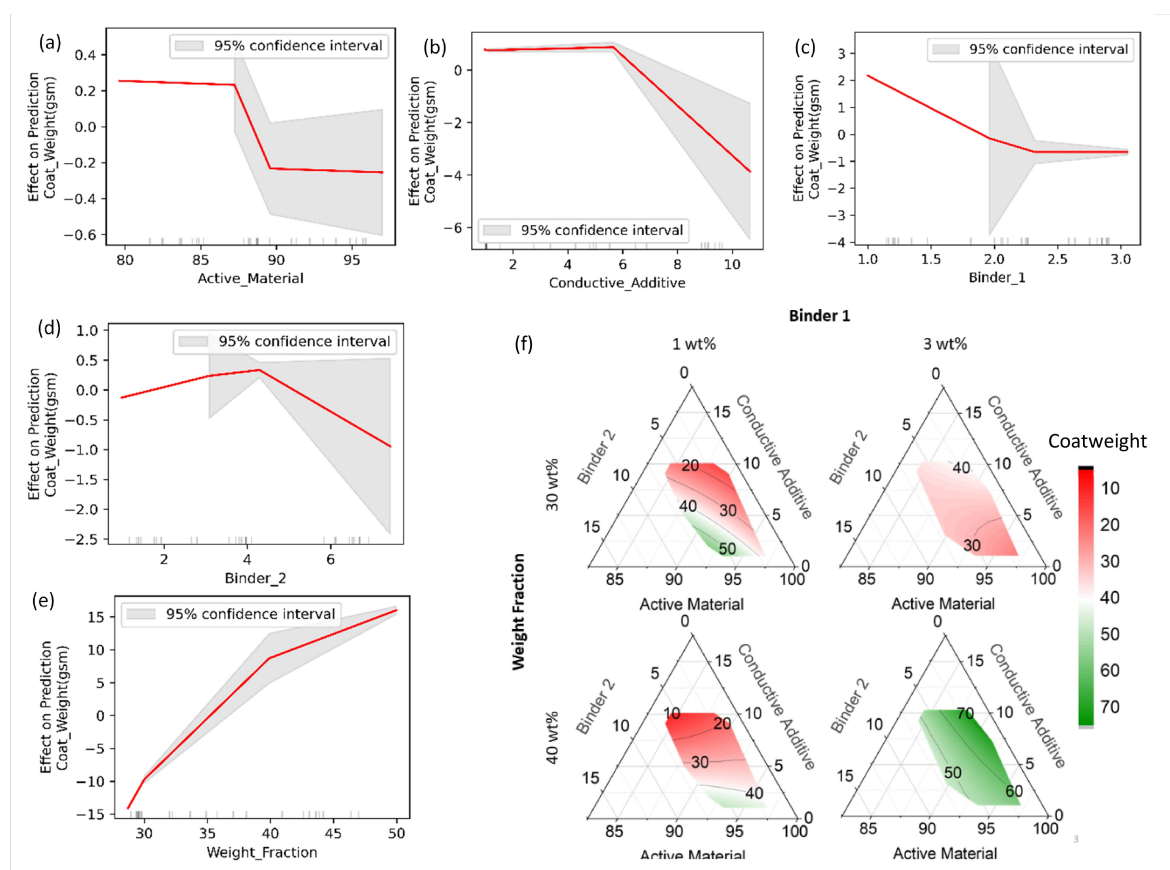


**Figure 9.** First order (a–e) and higher order (f) impact of slurry control variables on the coat weight

with weight percentage (Figure 10(b)). Weight fraction has a slight negative effect on adhesion (Figure 10(e)), while Binder 1, CMC, Figure 10(c), shows a minimum in adhesion at intermediate weight percentages. Active material also shows relatively little effect except at very high values (Figure 10(a)). MLR shows a similar trend, where binder 2 dominates the adhesion, universally increasing adhesion across the parameter space, this is visible on Figure 9(f).

The dependency of adhesion on SBR, the rubber binder is expected. The adhesion dependencies observed for the other components can usually be ascribed to their effect on the SBR distribution in the electrode. The carbon black, which tends to agglomerate in water,<sup>[58,61]</sup> promotes co-agglomeration with the SBR at high concentrations, making it less well distributed in the electrode. Higher weight fraction slurries also have higher coatweight and for thicker coatings, adhesion is known to decrease as uniform distribution of binder is harder to achieve and maintain throughout drying.<sup>[62]</sup> Active material only has an effect when it is so high there that there is less space in formulation for SBR.

While CMC in solution acts to thicken and increase dispersion, it is crystalline when dried<sup>[63]</sup> which makes the electrode more brittle and reduces adhesion. The reason for the increase at high amounts is unclear, one possibility is the high slurry viscosity impeding migration of SBR from the interface during drying, leading to more SBR near the current collector

interface and better adhesion. The effect of viscosity on binder migration has not been mapped out explicitly in the literature for battery electrode slurries, however in models for binder migration the viscosity term slows diffusion.<sup>[64,65]</sup>

As Figure 11 shows, the largest impact to the conductivity comes from the weight fraction, which decreases the measured conductivity, Figure 11(e). Conductive additive increases conductivity, Figure 11(b), where CMC reduces the conductivity at high weight percentages, Figure 11(c).

MLR via Figure 10(f) shows similar trends. Weight fraction has a negative effect on the conductivity at all mixture compositions. Increasing binder 2 also increases conductivity, while increasing either CMC or the active material decreases conductivity.

This conductivity was measured on current collector (which is highly conductive), hence it does not represent the conductivity of the coating alone and will depend highly on how efficiently current can flow through the coating to the current collector, and on the properties of the current collector-coating interface. It therefore is expected to follow the trends in adhesion, and this explains the relationship with SBR, which is perhaps counter-intuitive, as addition of non-conducting SBR results in an increase in conductivity. This is because the improved adhesion and better contact of the coating with the current collector. The change flattens at medium percentages

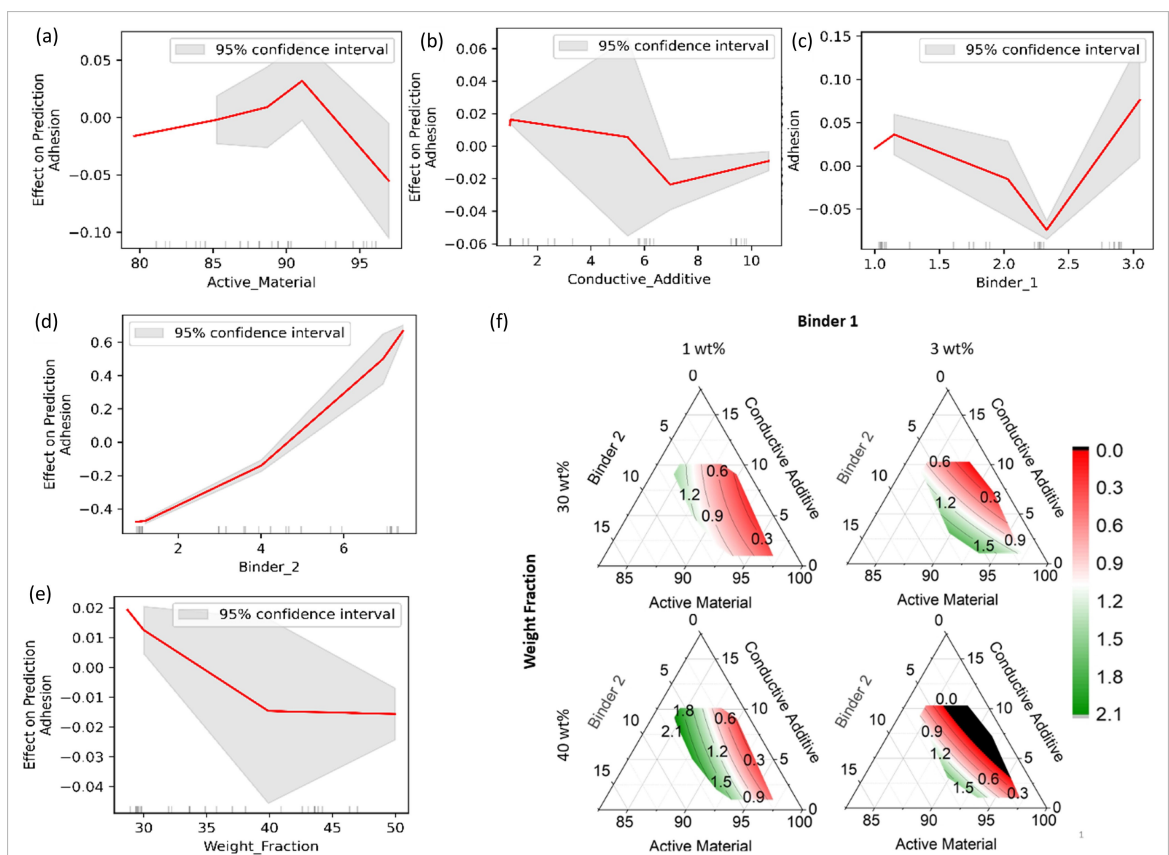


Figure 10. First order (a–e) and higher order (f) impact of slurry control variables on the peel adhesion force.

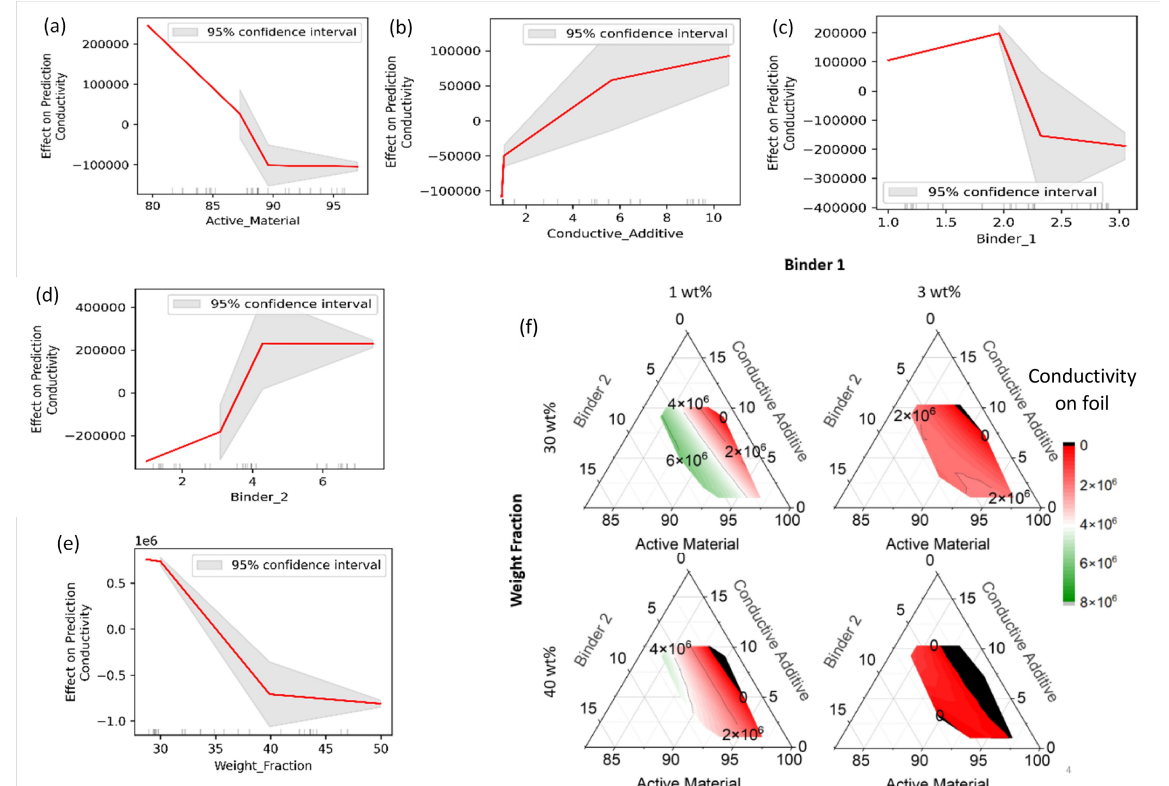


Figure 11. First order (a–e) and higher order (f) impact of slurry control variables on the coating conductivity measured on foil.

of SBR, when the effects of improved adhesion start to compete with the reduction in conductivity in the coating.

Conductive additive, as expected increases coating conductivity and thus the conductivity measured, but this is a smaller effect than the properties that effect the coating-current collector interface. The decrease in conductivity with weight fraction follows the trend in adhesion, Figure 9(d), where the increase in coatweight leads to less uniform distribution of SBR and thus poorer current collector-coating contact. CMC thickens the slurry, reducing mixing efficiency and impeding dispersion of SBR (for interface adhesion) and carbon black (for coating conductivity).

It is surprising that the properties of the coating-current collector interface dominate this measurement so heavily, and parameters that affect the coating conductivity (e.g., conductive additive) have smaller effects. This highlights the need for measurements on non-conductive substrates if the true coating conductivity is to be probed, but also shows that measurements on current collector have a unique ability to probe the interface.

The impact of the formulation on the cell discharge capacity is shown in Figure 12. Gravimetric capacity is used (in mAh/g) based on the active mass, to account for the difference in coatweight between the electrodes as well as the differences in formulation. Weight fraction has the most significant impact on the value of the discharge gravimetric capacity of the cell, Figure 12(e). With a higher percent of weight fraction the discharge gravimetric capacity increases. Binder 2 (SBR), Figure 12(d) shows the second most significant impact, having a

negative effect on the cell capacity, where Binder 1 (CMC) provides a small increase in capacity. Other factors show smaller impacts, Active material has a direct linear relation, serving to increase the capacity. Conductive additive shows relatively little effect until ~6%, which is same point at which it starts to increase the viscosity. The MLR via Figure 12(f) also shows similar results. At higher values of weight fraction and across the range of Binder 1, a smaller ratio of binder 2 and higher values of conductive additive plus active material means a higher discharge capacity.

The positive effect of weight fraction is interesting because it shows that high weight fractions are not just desirable because they reduce energy and time required for drying, but also have a positive impact on the electrochemistry. Weight fraction and CMC content are the viscosity-increasing factors, which provide the benefits of hindering migration during drying, prevent spreading of slurry on the surface of the current collector, and reducing settling of components in the slurry.

Over-incorporation of SBR is known to hinder the electrochemistry by slowing of electron transport. This shows the gains that can be achieved by reducing the SBR content and looking towards alternative methods for improving the mechanical properties of the coating.

Reaching the percolation concentration for Carbon Black has a negative impact on the electrochemistry, despite the viscosity increase being favourable. As discussed, agglomerates form above this concentration, that are difficult to disperse uniformly and may settle out during standing of the slurry/coating, leading to non-uniform coatings.

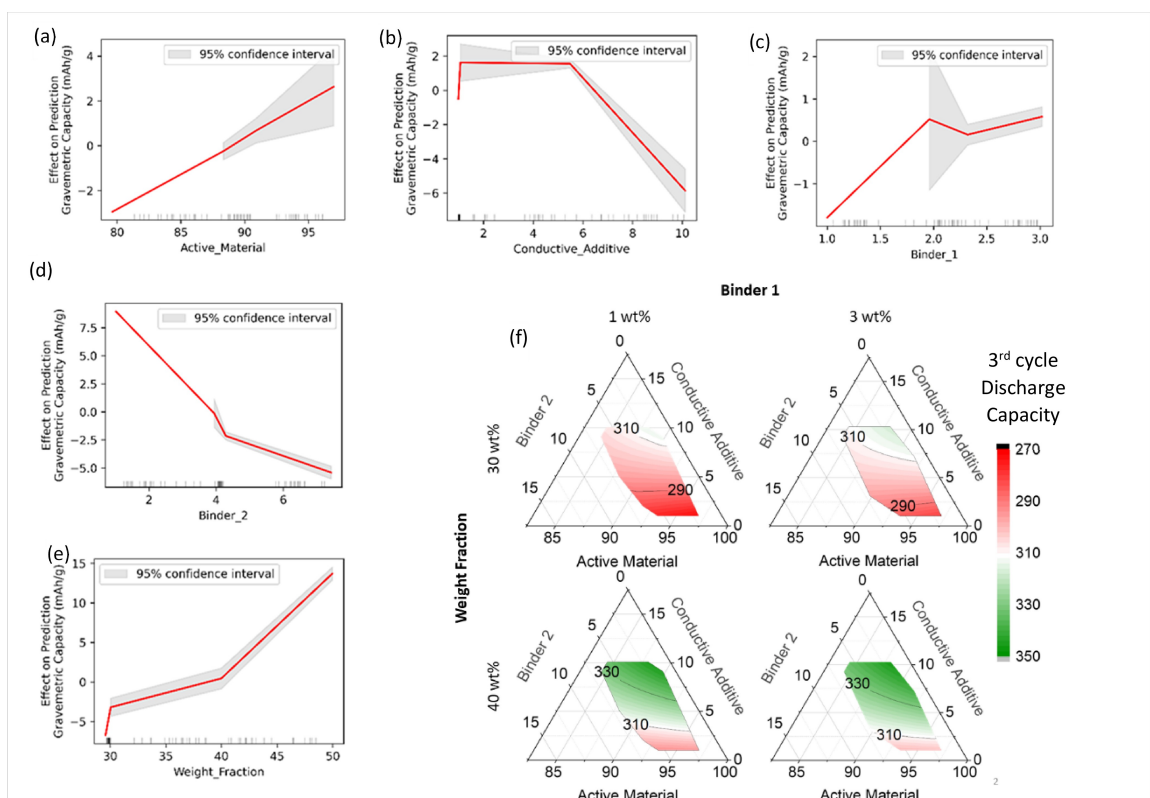


Figure 12. First order (a–e) and higher order (f) impact of slurry control variables on 3rd cycle discharge capacity of cells.

## Summary

Overall, several key dependencies and recommendations are identified in this study. The slurry viscosity is an important consideration which contributes to many of the other parameters. CMC contributes most to the slurry viscosity, as expected, however, carbon black and SBR, which are assumed not to contribute to slurry rheology in water, actually increase the viscosity at high concentrations. The high weight percentages are above those used in industry but are commonly utilised in research. The slurry structure can be very different when moving to lower weight percentages of carbon black and SBR and so this raises an important point and consideration for scaleup of battery research to industry.

Adhesion is mostly determined by SBR content, but interesting co-dependencies are observed, where high slurry viscosity may improve SBR dispersion and impede binder migration resulting in better adhesion. A surprising result observed in the conductivity data indicated that SBR improved the conductivity on current collector. This is due to the measurement technique and likely measurements on non-conductivity substrate would show the opposite trend. However, it highlights that conductivity on current collector is a useful parameter for studying the coating-current collector interface and, should be added to the toolbox for electrode characterisation.

Cell capacity improved in higher viscosity formulations, with high weight percentage and CMC content. This is likely due to the combined benefits of better suspension in the slurry, reducing spread on the current collector surface, and hindering component migration during drying, all of which contribute to a more uniform structure. Non-conductive SBR had a negative impact on capacity and reduction of SBR content is highlighted as a path towards performance improvements. Carbon Black, despite promoting conductivity, lowered capacity beyond its overlap concentration, suggesting that the overlapping structures of carbon black in the slurry are detrimental to the electrochemistry. Care therefore needs to be taken that the amount of carbon black used is not excessive, especially when attempting to reduce solvent content, which will increase the CB% in solution.

As viscosity is highly influential upon the performance properties of the electrode, future work should evaluate the rheology more completely. Differences between shear and extension are shown to give insights into the slurry structure, but evaluation of more subtleties in the rheology, shear rate dependant flow curves, or elastic and viscous moduli extracted from oscillatory tests, could provide greater information upon the impact upon properties such as capacity, adhesion and conductivity. Additionally, model testing on data from larger manufacturing lines is important for scalability. Finally, the approach demonstrated here for graphite anodes could be applied to other chemistries such as lithium ion cathodes and sodium ion electrodes. Another direction is to improve the accuracy of predictive models including responses such as adhesion and conductivity. In terms of the data analysis,

expanding the explainability to quantified importance of the features is also suggested for follow up studies.

## Conclusions

The formulation dependence of slurry and coating properties has been explored for a water-based graphite anode system, utilising an affordable set of experiments via a systematic DoE and machine learning to draw out key dependencies and isolate the response from individual variables. The value of a combined experimental-statistical approach is demonstrated, using experimental design and data extraction to systematically study relationships in battery manufacturing. The results showed both expected and more subtle relationships. The importance of the slurry rheology is highlighted, as shear and extensional viscosity are linked to electrode conductivity, adhesion, and final cell capacity. This demonstrates the importance of optimising the slurry rheology, which is often ignored, to obtain good final cell performance. Formulations with lower, industry-typical levels of binder and conductive additive, showed dramatically different behaviour to those with higher, research-typical, contents where additional material interactions form in the slurry. These highlight the very different material structures between research and industrial slurries, and suggest that care that must be taken to ensure research is scalable. Many additional subtle relationships highlight the importance of manufacturing parameters on the electrode and cell. It is crucial to bear in mind these interrelationships while optimizing industrial production systems and developing new technologies, as overlooking the proper tuning of the manufacturing process could lead to missed opportunities.

## Funding

This research was undertaken as part of the NEXTRODE project, funded by the Faraday Institution, UK. Grant Number: FIRG015.

## Author Contributions

C. D. Reynolds: Conceptualization, Methodology, Investigation, Data Curation, Formal Analysis, Validation, Writing – original draft. M. Faraji Niri: Conceptualization, Methodology, Software, Investigation, Formal analysis, Validation, Writing – original draft. M. F. Hidalgo: Software, Investigation, Writing – original draft. R. Heymer: Software, Visualization. L. A. Roman: Conceptualization, Methodology, FormalAnalysis. G. Alsofi: Data Curation, Formal Analysis, Writing – review and editing H. Khanom: Data Curation, Writing – review and editing B. Pye: Data Curation, Formal Analysis J. Marco: Funding acquisition, Supervision, Resources, Writing – review and editing, E. Kendrick: Conceptualization, Funding acquisition, Supervision, Resources, Writing – review and editing.

## Acknowledgements

The authors would like to acknowledge the support of the Battery Manufacturing Scale Up Line in WMG for assisting with the cell testing.

## Conflict of Interests

The authors declare that there is no known competing financial interests or personal relationships that could have appeared to influence the work reported in this paper.

## Data Availability Statement

The data that support the findings of this study are available in the supplementary material of this article.

**Keywords:** Battery Electrode Manufacturing • Data Science • Lithium-ion • Formulation • Slurry Properties

- [1] "Lithium-ion Battery Pack Prices Rise for First Time to an Average of \$151/kWh," can be found under [https://about.bnef.com/blog/lithium-ion-battery-pack-prices-rise-for-first-time-to-an-average-of-151-kwh/, 2022.](https://about.bnef.com/blog/lithium-ion-battery-pack-prices-rise-for-first-time-to-an-average-of-151-kwh/)
- [2] Y. Liu, R. Zhang, J. Wang, Y. Wang, *iScience* **2021**, *24*, 102332.
- [3] A. Kwade, W. Haselrieder, R. Leithoff, A. Modlinger, F. Dietrich, K. Droeder, *Nat. Energy* **2018**, *3*, 290–300.
- [4] C. Yuan, Y. Deng, T. Li, F. Yang, *CRP Ann.* **2017**, *66*, 53–56.
- [5] E. Kendrick, in *Future Lithium-Ion Batter.*, **2019**, pp. 262–289.
- [6] C. D. Reynolds, P. R. Slater, S. D. Hare, M. J. H. Simmons, E. Kendrick, *Mater. Des.* **2021**, *209*, 109971.
- [7] M. Faraji Niri, C. Reynolds, L. A. Román Ramírez, E. Kendrick, J. Marco, *Energy Storage Mater.* **2022**, *51*, 223–238.
- [8] K. Liu, M. F. Niri, G. Apachitei, M. Lain, D. Greenwood, J. Marco, *Control Eng. Pract.* **2022**, *124*, 105202.
- [9] L. A. Román-Ramírez, G. Apachitei, M. Faraji-Niri, M. Lain, D. Widanage, J. Marco, *Int. J. Energy Environ. Eng.* **2022**, *13*, 943–953.
- [10] M. F. V. Hidalgo, G. Apachitei, D. Dogaru, M. Faraji-Niri, M. Lain, M. Copley, J. Marco, *J. Power Sources* **2023**, *573*, 233091.
- [11] M. Faraji Niri, G. Apachitei, M. Lain, M. Copley, J. Marco, *Energy Technol.* **2022**, *10*, 2200893.
- [12] E. N. Primo, M. Chouchane, M. Touzin, P. Vazquez, A. A. Franco, *J. Power Sources* **2021**, *488*, 229361.
- [13] J. Xu, D. Z. Dominguez, A. Demortiere, A. A. Franco, *ECS Meet. Abstr.* **2023**, *MA2023-01*, 707.
- [14] L. A. Román-Ramírez, G. Apachitei, M. Faraji-Niri, M. Lain, W. D. Widanage, J. Marco, *J. Power Sources* **2021**, *516*, 230689.
- [15] A. El Malki, M. Asch, O. Arcelus, A. Shodiev, J. Yu, A. A. Franco, *J. Power Sources Adv.* **2023**, *20*, 100114.
- [16] J. B. Dunn, C. James, L. Gaines, K. Gallagher, Q. Dai, J. C. Kelly, *Material and Energy Flows in the Production of Cathode and Anode Materials for Lithium Ion Batteries*, **2015**.
- [17] Y. Zhang, J. Bailey, Y. Sun, A. Boyce, W. Dawson, C. Reynolds, Z. Zhang, X. Lu, P. Grant, E. Kendrick, P. Shearing, D. Brett, *J. Mater. Chem. A* **2022**, *10*, 10593–10603.
- [18] S. X. Drakopoulos, A. Gholamipour-Shirazi, P. MacDonald, R. C. Parini, C. D. Reynolds, D. L. Burnett, B. Pye, K. B. O'Regan, G. Wang, T. M. Whitehead, G. J. Conduit, A. Cazacu, E. Kendrick, *Cell Rep. Phys. Sci.* **2021**, *2*, 100683.
- [19] M. Wang, D. Dang, A. Meyer, R. Arsenault, Y.-T. Cheng, *J. Electrochem. Soc.* **2020**, *167*, 100518.
- [20] D. Grießl, A. Adam, K. Huber, A. Kwade, *J. Electrochem. Soc.* **2022**, *169*, 020531.
- [21] J. Entwistle, R. Ge, K. Pardikar, R. Smith, D. Cumming, *Renewable Sustainable Energy Rev.* **2022**, *166*, 112624.
- [22] X. Lu, S. R. Daemi, A. Bertei, M. D. R. Kok, K. B. O'Regan, L. Rasha, J. Park, G. Hinds, E. Kendrick, D. J. L. Brett, P. R. Shearing, *Joule* **2020**, *4*, 2746–2768.
- [23] P. S. Grant, D. Greenwood, K. Pardikar, R. Smith, T. Entwistle, L. A. Middlemiss, G. Murray, S. A. Cussen, M. J. Lain, M. J. Capener, M. Copley, C. D. Reynolds, S. D. Hare, M. J. H. Simmons, E. Kendrick, S. P. Zankowski, S. Wheeler, P. Zhu, P. R. Slater, Y. S. Zhang, A. R. T. Morrison, W. Dawson, J. Li, P. R. Shearing, D. J. L. Brett, G. Matthews, R. Ge, R. Drummond, E. C. Tredenick, C. Cheng, S. R. Duncan, A. M. Boyce, M. Faraji-Niri, J. Marco, L. A. Roman-Ramirez, C. Harper, P. Blackmore, T. Shelley, A. Mohsseni, D. Cumming, *J. Phys. Energy* **2022**, *4*, 042006.
- [24] M. Faraji Niri, K. Aslansefat, S. Haghi, M. Hashemian, R. Daub, J. Marco, *Energies* **2023**, *16*, 6360.
- [25] T. Lombardo, M. Duquesnoy, H. El-Bouysidy, F. Åren, A. Gallo-Bueno, P. B. Jørgensen, A. Bhowmik, A. Demortière, E. Ayerbe, F. Alcaide, M. Reynaud, J. Carrasco, A. Grimaud, C. Zhang, T. Vegge, P. Johansson, A. A. Franco, *Chem. Rev.* **2022**, *122*, 10899–10969.
- [26] S. Haghi, M. F. V. Hidalgo, M. F. Niri, R. Daub, J. Marco, *Batteries & Supercaps* **2023**, *6*, e202300046.
- [27] R. Ge, D. J. Cumming, R. M. Smith, *Powder Technol.* **2022**, *403*, 117366.
- [28] A. Hoffmann, S. Spiegel, T. Heckmann, P. Schäfer, W. Schabel, *J. Coat. Technol. Res.* **2022**, *20*, 3–14, DOI 10.1007/s11998-022-00660-8.
- [29] M. Aykol, P. Herring, A. Anapolsky, *Nat. Rev. Mater.* **2020**, *5*, 725–727.
- [30] X. Chen, X. Liu, X. Shen, Q. Zhang, *Angew. Chem. Int. Ed.* **2021**, *60*, 24354–24366.
- [31] L. A. Román-Ramirez, J. Marco, *Appl. Energy* **2022**, *320*, 119305.
- [32] J. Benesty, J. Chen, Y. Huang, I. Cohen, in *Noise Reduct. Speech Process.* (Eds.: I. Cohen, Y. Huang, J. Chen, J. Benesty), Springer, Berlin, Heidelberg, **2009**, pp. 1–4.
- [33] T. Hastie, R. Tibshirani, J. Friedman, *The Elements of Statistical Learning*, Springer, New York, NY, **2009**.
- [34] S. R. Safavian, D. Landgrebe, *IEEE Trans. Syst. Man Cybern.* **1991**, *21*, 660–674.
- [35] O. Badmos, A. Kopp, T. Bernthal, G. Schneider, *J. Intell. Manuf.* **2020**, *31*, 885–897.
- [36] C. Molnar, *Interpretable Machine Learning: A Guide for Making Black Box Models Interpretable*, Lulu, Morrisville, North Carolina, **2019**.
- [37] D. W. Apley, J. Zhu, *J. R. Stat. Soc. Ser. B Stat. Methodol.* **2020**, *82*, 1059–1086.
- [38] M. F. Niri, G. Apachitei, M. Lain, M. Copley, J. Marco, *J. Power Sources* **2022**, *549*, 232124.
- [39] M. J. Anderson, P. J. Whitcomb, M. A. Bezener, *Formulation Simplified: Finding the Sweet Spot through Design and Analysis of Experiments with Mixtures*, Taylor & Francis, New York, **2018**.
- [40] G. E. P. Box, J. S. Hunter, W. G. Hunter, *Statistics for Experimenters: Design, Innovation, and Discovery*, 2nd Edition | Wiley, Wiley, **2005**.
- [41] D. C. Montgomery, E. A. Peck, G. G. Vining, *Introduction to Linear Regression Analysis*, John Wiley & Sons, **2021**.
- [42] M. Drews, S. Tepner, P. Haberzettl, H. Gentischer, W. Beichel, M. Breitwieser, S. Vierrath, D. Biro, *RSC Adv.* **2020**, *10*, 22440–22448.
- [43] W. Zhu, J. Zhou, S. Xiang, X. Bian, J. Yin, J. Jiang, L. Yang, *Front. Chem.* **2021**, *9*, 712225, <https://www.frontiersin.org/articles/10.3389/fchem.2021.712225/full>.
- [44] M. Zarei-Jelyani, M. Babaiee, S. Baktashian, R. Eqra, *J. Solid State Electrochem.* **2019**, *23*, 2771–2783.
- [45] C. D. Reynolds, J. Lam, L. Yang, E. Kendrick, *Mater. Des.* **2022**, *222*, 111104.
- [46] B. Hallmark, M. Bryan, E. Bosson, S. Butler, T. Hoier, O. Magens, N. Pistre, L. Pratt, B.-A. Ward, S. Wibberley, D. I. Wilson, *Meas. Sci. Technol.* **2016**, *27*, 125302.
- [47] S. Kowalski, J. A. Cornell, G. Geoffrey Vining, *Commun. Stat. – Theory Methods* **2000**, *29*, 2255–2280.
- [48] H. Bozdogan, *Psychometrika* **1987**, *52*, 345–370.
- [49] M. Seeger, *Int. J. Neural Syst.* **2004**, *14*, 69–106.
- [50] C. E. Rasmussen, H. Nickisch, *J. Mach. Learn. Res.* **2010**, *11*, 3011–3015.
- [51] C. E. Rasmussen, C. K. I. Williams, *Gaussian Processes for Machine Learning*, MIT Press, Cambridge, Mass., **2006**.
- [52] R. R. Richardson, C. R. Birk, M. A. Osborne, D. A. Howey, *IEEE Trans. Ind. Inform.* **2019**, *15*, 127–138.
- [53] D. Yang, X. Zhang, R. Pan, Y. Wang, Z. Chen, *J. Power Sources* **2018**, *384*, 387–395.
- [54] T. Fushiki, *Stat. Comput.* **2011**, *21*, 137–146.
- [55] W. Bauer, D. Nötzel, *Ceram. Int.* **2014**, *40*, 4591–4598.
- [56] W. B. Hawley, J. Li, *J. Energy Storage* **2019**, *25*, 100862.

- [57] L. Ouyang, Z. Wu, J. Wang, X. Qi, Q. Li, J. Wang, S. Lu, *RSC Adv.* **2020**, *10*, 19360–19370.
- [58] C. D. Reynolds, S. D. Hare, P. R. Slater, M. J. H. Simmons, E. Kendrick, *Energy Technol.* **2022**, *10*, 2200545.
- [59] M. Youssry, F. Z. Kamand, M. I. Magzoub, M. S. Nasser, *RSC Adv.* **2018**, *8*, 32119–32131.
- [60] S. Subramanian, G. Øye, *Colloid Polym. Sci.* **2021**, *299*, 1223–1236.
- [61] A. Basch, R. Horn, J. O. Besenhard, *Colloids Surf. Physicochem. Eng. Asp.* **2005**, *253*, 155–161.
- [62] W. Haselrieder, B. Westphal, H. Bockholt, A. Diener, S. Höft, A. Kwade, *Int. J. Adhes. Adhes.* **2015**, *60*, 1–8.
- [63] P. Basu, U. Narendrakumar, R. Arunachalam, S. Devi, I. Manjubala, *ACS Omega* **2018**, *3*, 12622–12632.
- [64] F. Font, B. Protas, G. Richardson, J. M. Foster, *J. Power Sources* **2018**, *393*, 177–185.
- [65] C. Zihrlul, M. Lippke, A. Kwade, *Batteries* **2023**, *9*, 455.

Manuscript received: November 3, 2023

Revised manuscript received: December 6, 2023

Accepted manuscript online: December 7, 2023

Version of record online: December 21, 2023